

Title: Observation of generic $U(m)$ non-Abelian holonomy in photonics

Authors: Youlve Chen¹, Jinlong Xiang¹, An He¹, Yikai Su¹, Ian H. White^{2,3} and Xuhan Guo^{1*}

Affiliations:

¹State Key Laboratory of Photonics and Communications, School of Information and Electronic Engineering, Shanghai Jiao Tong University; Shanghai, 200240, China.

²Centre for Photonic Systems, Department of Engineering, University of Cambridge; Cambridge, UK

³University of Bath; Bath, UK

*Corresponding author. Email: guoxuhan@sjtu.edu.cn

Abstract: Non-Abelian geometric phases form the foundation of fault-tolerant holonomic quantum computation. An 'all-geometric' approach leveraging these phases enables robust unitary operations in condensed matter systems. Photonics, with rich degrees of freedom, offer a highly promising platform for non-Abelian holonomy. Yet, achieving universal unitary transformations in photonic holonomy remain elusive. Intrinsic positive real couplings in dissipationless photonic waveguides restrict holonomy to special orthogonal matrices, falling short of universal quantum gates or arbitrary linear operations. Here, we introduce artificial gauge fields (AGFs) to enable complex-valued couplings, expanding photonic holonomy to the full unitary group. We realize generic $U(2)$ transformations and synthesize higher-dimensional $U(m)$ operations (up to $U(4)$) in integrated photonics. Our results open doors toward the transformative 'all-geometric-phase' approach in photonic computing in both classical and quantum realms.

Main Text:

Non-Abelian geometric phase is a generalization of the scale Pancharatnam–Berry phase(1, 2), which arises from the parallel transport of a set of degenerate states around a closed loop in parameter space(3). It enables robust, fluctuation-resilience unitary transformations and is considered as the foundation of holonomic quantum computation(4). As the salient ingredient of the 'all-geometric' approach(5, 6) to quantum computation, non-Abelian holonomy has been utilized to implement universal quantum gates in various condensed matter platforms, including cold atoms(7-9), superconducting circuits(10-12), trapped ions(5, 13) and nitrogen vacancy centers(6, 14-16). Recently, classical wave flux, such as light and sound that possess additional internal degrees of freedom, become an emerging platform for exploring non-Abelian holonomy. Judicious manipulation of Hamiltonian with chiral symmetry in acoustic(17, 18) and photonics(19-26) can generate the matrix-valued non-Abelian geometric phase. However, the universal transformation, which is the central requirement of universal quantum gates or arbitrary classical linear computing tasks, remains out of reach for the non-Abelian geometric phase in photonics. Existing photonic holonomy can only provide a single type of rotation ($e^{i\alpha\sigma_y}$) between two modes, resulting the representational scope is limited to special orthogonal group ($SO(m)$) (19, 21, 22, 24, 25), which can only perform specific tasks such as braiding or special orthogonal matrices. This is due to the intrinsic positive-valued couplings between dissipationless optical waveguides, which constrains the available degrees of freedom in the parameter space. Therefore, realizing full unitary

group ($U(m)$) holonomy is the key ingredient of the all-geometric’ approach for both classical and quantum photonic computing.

Generic $U(m)$ holonomic gates in photonics hinges on generating arbitrary complex-valued couplings—a capability available to electrons in condensed matter physics(5, 6, 10, 12, 15, 16) but profoundly challenging for photons. Artificial gauge fields (AGFs), implemented through periodic modulation within the framework of Floquet engineering to synthesize the effective electromagnetic fields, offer the solution. In photonics, AGFs are typically realized through periodically modulated waveguides, such as helically bent structures. These have been successfully employed to manipulate light guiding(27, 28), and engineer photonic topological bands such as Floquet topological insulators(29-33). More recently, AGFs have been applied to control anomalous coupling behaviors between integrated waveguides, such as dispersionless coupling(34, 35) and suppression of coupling (zero coupling)(36, 37).

In this work, we propose a generic framework that can design arbitrary $U(m)$ non-Abelian geometric phase in photonics: we realize complex-valued couplings based on artificial gauge fields by employing periodically bent waveguides, analogous to the complex hopping of electrons in the presence of an external magnetic field. This strategy offers novel insights into the manipulation of optical dynamics. The engineered complex couplings are further introduced into a four-waveguide system with chiral symmetry. By gradually tuning the bending amplitude and period, both the modulus and argument of the complex coupling can evolve adiabatically, enabling the construction of a $U(2)$ holonomy. Any $U(2)$ matrix can be decomposed into fundamental rotations generated by Pauli matrices σ_z , σ_y , and a global phase induced by the identity matrix I . Among these, the rotation generated by σ_y has been previously realized using positive-valued couplings(21, 22, 25); the rotation generated by σ_z , and the global phase induced by I , which require complex-valued couplings, are realized by inducing Berry phases for two degenerate modes. We experimentally demonstrate these building blocks, and also realize an ordinary $U(2)$ transformation that combines different types of rotations. Non-Abelian characteristics of $U(2)$ is also demonstrated. Furthermore, higher-dimensional $U(m)$ matrices can be systematically synthesized through cascaded and parallel combinations of $U(2)$ transformations, following the framework of Givens rotations(38). Especially, integrated photonics provides a scalable platform for high-dimensional holonomy. As a proof of concept, we also experimentally implement a $U(4)$ matrix. Our work enables non-Abelian geometric phase to be applicable for arbitrary linear optical computing tasks, opening new avenues for the robust, all-geometric-phase-based classical and quantum computing in photonics.

Artificial gauge fields induce complex coupling

The coupling coefficient between two dissipationless straight waveguides is a positive number, originating from the mode overlap with dielectric perturbation(39). Therefore, the Berry-Wilzeck-Zee (BWZ) connection is proportional to σ_y , which restricts the non-Abelian geometric phase to $SO(2)$ group ($e^{i\alpha\sigma_y}$) in photonics. The further realization of full $U(2)$ group requires more varieties of rotations such as generated by σ_z , σ_x , and the global phase induced by identity matrix I . Achieving such transformations necessitates the introduction of complex-valued coupling coefficients.

To address this problem, we employ periodic bent waveguides to introduce the AGFs, thereby enabling effective complex couplings. This effective coupling coefficient is reciprocal ($\kappa_{AB} = \kappa_{BA}^\dagger$), and the system is Hermitian. Taking advantage of the high-index contrast of integrated photonics, silicon waveguides can bear very sharp bending with low loss(40), which facilitates to realize the periodic driving of bendings to introduce AGFs(34-37). We begin our analysis with the complex coupling between two waveguides. The effective complex couplings between two

identical periodic bent waveguides can be expressed as: $\kappa_{\text{bend}} = \frac{\kappa_{\text{straight}}}{P} \int_0^P e^{-i\beta g \frac{dx_0(z)}{dz}} dz = |\kappa_{\text{bend}}| e^{i\varphi}$ (34, 41, 42). Where the bending profile is denoted by $x_0(z)$ with a period P . The symbol g denotes the center-to-center separation between two waveguides, κ_{straight} represents the coupling between two straight waveguides with the same center-to-center separation g , and β is the propagation constant; the detailed derivation can be found in the Supplementary Text (ST1). It can be observed that κ_{bend} can be a complex number (Eq. S8), and the argument and modulus of κ_{bend} can be modulated by the period, amplitude of bending profile $x_0(z)$, as derived in Eq. S9. We simulate different $x_0(z)$ and make a comparison with the coupling between straight waveguides. In two straight waveguides with positive-valued coupling, the phase difference between to waveguide is exactly $\pi/2$ (Eq. S8 with $\varphi=0$). While for AGFs induced complex-valued coupling, the phase between to waveguides varies from $0 \sim \pi$ (Eq. S8 and Fig. S2B-D). The theoretical calculation and FDTD simulation fit well with each other (Fig. S2A).

We now turn to the implementation of complex coupling in a three-waveguide stimulated Raman adiabatic passage (STIRAP) system(43-47), whose zero mode plays a crucial role in constructing non-Abelian holonomy. As discussed in Supplementary Text (ST2), in the conventional STIRAP with positive-valued coupling coefficients, the phase difference in the two outer waveguides is exactly π when the zero mode is excited (Fig. S5A). In contrast, for STIRAP systems incorporating complex-valued couplings, the phase difference in two outer waveguides is not π (Fig. S5B-D), and is directly determined by the argument of the complex coupling. The simulation results are in agreement with the theoretical predictions.

U(2) holonomy

We now incorporate complex coupling into the realization of holonomy. The adiabatic evolution of complex-valued coupling can be precisely controlled by gradually varying the amplitude, period, and profile of bending. Both the modulus and argument of complex coupling can be adiabatically modulated to accomplish a holonomy. As Fig. 1A shows, the holonomy device is comprised of four periodic bent silicon waveguides on two layers. All four waveguides have an identical bending profile $x_0(z)$, as AGF-induced coupling necessitates that the surrounding waveguides (A, B, C) maintain the same bending geometry as the central waveguide X. Moreover, having a uniform bending profile ensures no relative dynamic phase accumulation or relative loss among the waveguides, which can be eliminated under gauge transformation. Thus, the coupling between waveguides B and X, C and X are complex-valued due to the induced AGFs. To be specific, the coupling between waveguides A, X is a positive real number since the displacement is zero ($g=0$) in the direction of AGF (Fig. S4 and discussed in ST1). Thus, the Hamiltonian can be written as:

$$H(z) = \begin{bmatrix} \beta & |\kappa_{AX}| & |\kappa_{BX}| e^{i\varphi_{BX}} & |\kappa_{CX}| e^{i\varphi_{CX}} \\ |\kappa_{AX}| & \beta & 0 & 0 \\ |\kappa_{BX}| e^{-i\varphi_{BX}} & 0 & \beta & 0 \\ |\kappa_{CX}| e^{-i\varphi_{CX}} & 0 & 0 & \beta \end{bmatrix} \quad (1)$$

Where, $|\kappa_{iX}|$, φ_{iX} represent the modulus and argument of coupling, respectively. This Hamiltonian with chiral symmetry(48) supports two degenerate modes (Eq. S13). And the BWZ connection is also calculated in Eq. S15. Notably, the BWZ connection contains all three Pauli matrices ($\sigma_x, \sigma_y, \sigma_z$) as well as the identity matrix I , indicating that it can generate a U(2) holonomy. However, the expression is too complicated to directly map onto a holonomic path that realizes an arbitrary target matrix. Therefore, we aim to simplify the formulation and identify a generic framework that enables the systematic design of holonomic paths.

Generic U(2) matrix can be decomposed as four fundamental building blocks, fully containing four degrees of freedom for U(2) group(49):

$$U(2) = \exp(i\alpha_1 I) \cdot \exp[i\alpha_2 \sigma_z] \cdot \exp(i\alpha_3 \sigma_y) \cdot \exp[i\alpha_4 \sigma_z] \quad (2)$$

As illustrated in Fig. 1B, the U(2) rotation is visualized and decomposed on the Bloch sphere. The U(2) group can be expressed as the product of a U(1) phase factor ($e^{i\alpha_1 I}$) and the SU(2) group. The SU(2) group, which represents three-dimensional rotations, can be further decomposed into successive rotations around the z-axis ($e^{i\alpha_2 \sigma_z}$), y-axis ($e^{i\alpha_3 \sigma_y}$), and z-axis ($e^{i\alpha_4 \sigma_z}$)—commonly referred to as the z-y-z Euler-angle decomposition(50-54). Thus, realizing these fundamental building blocks and cascading them sequentially can construct generic U(2) holonomy. Among these rotations, $e^{i\alpha_3 \sigma_y}$ that belongs to SO(2) has been demonstrated in the reported scheme with positive-valued coupling. Next, we will discuss the other rotations by introducing the Berry phase for dark modes through complex coupling.

We start with analyzing the Berry phase acquired in a three-waveguide STIRAP process involving complex-valued couplings. As Fig. 2A shows, the dark mode $|D_2\rangle$ experiences a three-waveguide STIRAP process, and $|D_1\rangle$ resides in an isolated waveguide. $|D_2\rangle$ can be expressed as $|D_2\rangle = -e^{i\varphi_{CX}} \sin(\frac{\theta}{2})|A\rangle + \cos(\frac{\theta}{2})|C\rangle$. Where we define $\frac{\theta}{2} = \arctan(|\kappa_{CX}|/|\kappa_{AX}|)$. Thus, the Berry connection can be expressed as $A_{\varphi_{CX}} = i\langle D_2 | \partial_{\varphi_{CX}} D_2 \rangle = -\sin^2(\frac{\theta}{2})$, $A_\theta = i\langle D_2 | \partial_\theta D_2 \rangle = 0$, and there is a Berry phase $\oint -\sin^2(\frac{\theta}{2})d\varphi_{CX}$ acquired through the holonomy. It is evident that the corresponding Berry curvature can be analogous to the field of a magnetic monopole(55) with a charge of $-1/2$ located at the origin. Consequently, the Berry phase corresponds to negative half the solid angle α enclosed by the holonomic path on the Bloch sphere in Fig. 2A, and the star represents the start/end point of a holonomic path. An example of the simulated Berry phase, acquired through a holonomy in both Hilbert space and real space, is shown in Fig. S7 and discussed in ST2. In contrast, if the coupling is restricted to positive-valued, no geometric phase is accumulated over the two STIRAP processes, as the solid angle is zero (Fig. S6). Now we take the second degenerate dark mode $|D_1\rangle$ into consideration, this holonomy generates a basic unitary matrix of U(2) transformation for $|D_1\rangle$ and $|D_2\rangle$: $\begin{bmatrix} 1 & 0 \\ 0 & e^{-i\frac{\alpha}{2}} \end{bmatrix}$. This scheme enables the implementation of a variety of quantum gates, including the S gate, T gate, and R_k gate. Fig. 2A also shows an example of the measured and predicted elements of this building blocks, and the detailed parameters, including the gap distance between waveguides, bending profiles of waveguides, as well as the evolution of complex-valued couplings are shown in Fig. S8A. The fidelity $F=0.9427$, where, the fidelity is defined as $F= (1/N) |\text{Tr}(U_t^\dagger U_{\text{exp}})|$ (56-59) based on Frobenious inner product, $\text{Tr}(A)$ represents the trace of A , N is the dimension of the unitary matrix, U_t , U_{exp} are the theoretical and experimental unitary matrix, respectively.

If we also introduce the same Berry phase to $|D_1\rangle$, as illustrated in Fig. 2B, we cascade an identical STIRAP process for $|D_1\rangle$. The holonomic path of this STIRAP process for $|D_1\rangle$ in the Bloch sphere is also shown in Fig. 2B. In this way, both degenerate two modes acquire the same geometric phase. Consequently, a fundamental building block of the U(2) group: $e^{-i\frac{\alpha}{2}I} = \begin{bmatrix} e^{-i\frac{\alpha}{2}} & 0 \\ 0 & e^{-i\frac{\alpha}{2}} \end{bmatrix}$ is generated. Fig. 2B shows an example of this building blocks, the detailed parameters of the holonomy is shown in Fig. S8B. The fidelity between experimental results and theoretical prediction is 0.9288.

We now focus on the remaining building blocks of U(2) group in Eq. 2: $e^{i\alpha\sigma_z}$ and $e^{i\alpha\sigma_y}$. For the $e^{i\alpha\sigma_z}$ component, a straightforward approach is to introduce two Berry phases with opposite signs for $|D_1\rangle$ and $|D_2\rangle$, as the abovementioned method. However, in order to reduce the device length, we adopt another configuration. As illustrated in Fig. 2C, the structure is designed as $g_{BX} = g_{CX}$ and $\kappa_{BX} = \kappa_{CX}^\dagger$. Consequently, the BWZ connection in Eq. S15 can be significantly simplified, and the two degenerate modes $|D_1\rangle$ and $|D_2\rangle$ acquire geometric phases with identical absolute values but opposite signs (Eq. S17-S21). The geometric phase is the solid angle enclosed by the holonomic path on the Bloch sphere in Fig. 2C. As a result, a fundamental building block of U(2) transformation: $e^{i\alpha\sigma_z} = \begin{bmatrix} e^{i\alpha} & 0 \\ 0 & e^{-i\alpha} \end{bmatrix}$ is generated. An exemplified experimental and theoretical results of this rotation is shown in Fig. 2C, the detailed parameters of the holonomy is illustrated in Fig. S8C, and the fidelity is 0.9830.

We now address the final building block, $e^{i\alpha\sigma_y} = \begin{bmatrix} \cos(\alpha) & \sin(\alpha) \\ -\sin(\alpha) & \cos(\alpha) \end{bmatrix}$, which belongs to SO(2) group and has been demonstrated in reported schemes(21, 22, 25). In these configurations, three positive-valued couplings are isomorphic to a 2-sphere, and the corresponding geometric phase is determined by the solid angle α enclosed by the holonomic path on that sphere. The experimental and theoretical results are shown in Fig. 2D, and the fidelity is 0.9832.

Figure 2 also shows the experimentally measured intensity and phase of the aforementioned building blocks, as well as their theoretical predictions. Notably, we measure the detailed phase of individual matrix elements through the interference method (some phase values are labeled with "N/A" since their theoretical intensity is zero, rendering the phase devoid of physical meaning). For example, to measure the geometric phase of a beam undergoing the holonomy, we measure the phase difference between light propagating through the holonomy and that through an isolated reference waveguide (Fig. S9C-D). The reference waveguide shares the same bending profile as the holonomy waveguides and therefore accumulates the same dynamical phase. By measuring the relative phase between the two paths, we can extract the geometric phase of matrix elements eliminating the dynamical phase contribution. Besides, we also measure the relative phase between different matrix elements (Fig. S9A-B). More information about the interference measurement methodology can be found in Supplementary Text (ST4).

To ensure the completeness of the U(2) group representation, we refer to the Euler parametrization in Eq. 2. If $\alpha_1, \alpha_2, \alpha_4$ span the range from $-\pi$ to π , and α_3 covers the interval from $-\pi/2$ to $\pi/2$, this is sufficient to realize full coverage of U(2) group(50). The range of α_3 has been demonstrated in reported works. Negative values of α_1, α_2 , and α_4 can be implemented by simply exchanging P_1 and P_2 . Furthermore, larger effective rotation angles can be achieved by cascading multiple holonomic devices in sequence.

Here, we demonstrate a U(2) transformation that incorporate multiple types of rotations into a device, as shown in Fig. 3A. At step 1, $|D_1\rangle$ resides in the isolated waveguide B, while $|D_2\rangle$ experience a three-waveguide STIRAP process involving waveguide A, X, and C. κ_{CX} starts with a complex value, and adiabatically evolves to a positive valued. Therefore, $|D_2\rangle$ acquires a Berry phase. Step 2 involves all positive-valued coupling, and the BWZ connection is proportional to σ_y , contributing to an SO(2) rotation between $|D_1\rangle$ and $|D_2\rangle$. At step 3, $|D_2\rangle$ resides in the isolated waveguide C, while $|D_1\rangle$ experience a three-waveguide STIRAP process composed of waveguide A, X, and B. κ_{BX} starts with a positive value, and adiabatically evolves to a complex value. Thus, $|D_1\rangle$ acquires a Berry phase. The theoretically predicted and experimentally measured matrix elements are also shown in Fig. 3A-B.

To further illustrate the Abelian nature of $SO(2)$ and the non-Abelian character of $U(2)$, we perform cascaded holonomic operations. Figure 3C presents the composition of two successive $SO(2)$ rotations, which commute with each other, demonstrating the Abelian property. In contrast, Fig. 3D demonstrates the composition of a $U(2)$ and an $SO(2)$ rotation, which exhibits non-commutative behavior, confirming the non-Abelian nature of the $U(2)$ holonomy.

$U(m)$ holonomy

Any target $U(m)$ matrix can be decomposed into a cascade and parallel combination of $U(2)$ matrices using Givens rotations(38). As Fig. 4A shows, we exemplify a $U(3)$ matrix through a mesh comprised of three $U(2)$ matrices. The mathematical model, experimental results, and theoretical prediction are also shown in Fig. 4A, and the fidelity is 0.9832.

Figure 4B shows a $U(4)$ matrix through a mesh comprised of six $U(2)$ matrices. The mathematical model, experimental results, and theoretical prediction are also shown in Fig. 4B, and the fidelity is 0.9524. Here, we only measure the intensity of $U(m)$ elements since it is very challenging to conduct m^2 times of interference to acquire the phase of all elements.

Discussion and conclusion

The manipulation of dynamic and geometric phases plays a fundamental role in information processing within electronic and photonic systems. Compared with the dynamic phase, the ‘all-geometric’ approach brings the intrinsic robustness to quantum computation against the environmental noise and decoherence in condensed matter physics. As shown in Fig. S14A, the successful realization of $SU(m)$ or $U(m)$ groups has enabled fault-resilient universal holonomic quantum gates across various condensed matter platforms. Moreover, scalability remains a long-term goal for achieving efficient multi-qubit manipulation. While geometric-phase-based (holonomic) quantum computing has been well established in condensed matter systems, it has remained elusive in photonics, where most approaches rely on dynamic phase control — such as in Mach-Zehnder interferometer meshes(60), micro-ring resonator arrays(61), diffractive metasurfaces(62, 63), and intensity modulation(56, 64) schemes. As summarized in Fig. S14B, these systems typically operate at a single wavelength and have low fabrication tolerance due to their sensitivity to dynamic phase variations. In contrast, an all-geometric approach via holonomy in photonics provides broader bandwidth for high-dimensional matrices(25) and greater fabrication tolerance(25), as it relies only on the path in parameter space and benefits from adiabatic evolution.

In conclusion, we resolve the key issue of non-Abelian geometric phase in photonics— construction of generic unitary group to fulfill the demand of universal quantum gates or arbitrary classical linear computing task in photonics. Besides, the excellent scalability, and mass-production integrated photonic platform enables the large-scale computing networks. This work demonstrates the feasibility of implementing geometric-phase-based computing in photonic systems, opening a promising route toward inherently fault-tolerant photonic quantum computing and novel high-performance classical optical processors.

References and Notes

1. S. Pancharatnam, in *Proceedings of the Indian Academy of Sciences-Section A*. (Springer, 1956), vol. 44, pp. 247-262.

2. M. V. Berry, Quantal phase factors accompanying adiabatic changes. *Proceedings of the Royal Society of London. A. Mathematical and Physical Sciences* **392**, 45-57 (1984).
3. F. Wilczek, A. Zee, Appearance of Gauge Structure in Simple Dynamical Systems. *Physical Review Letters* **52**, 2111-2114 (1984).
4. C. Nayak, S. H. Simon, A. Stern, M. Freedman, S. Das Sarma, Non-Abelian anyons and topological quantum computation. *Reviews of Modern Physics* **80**, 1083-1159 (2008).
5. L.-M. Duan, J. I. Cirac, P. Zoller, Geometric manipulation of trapped ions for quantum computation. *Science* **292**, 1695-1697 (2001).
6. C. Zu *et al.*, Experimental realization of universal geometric quantum gates with solid-state spins. *Nature* **514**, 72-75 (2014).
7. Y. J. Lin, R. L. Compton, K. Jiménez-García, J. V. Porto, I. B. Spielman, Synthetic magnetic fields for ultracold neutral atoms. *Nature* **462**, 628-632 (2009).
8. J. Dalibard, F. Gerbier, G. Juzeliūnas, P. Öhberg, Colloquium: Artificial gauge potentials for neutral atoms. *Reviews of Modern Physics* **83**, 1523-1543 (2011).
9. F. Leroux *et al.*, Non-Abelian adiabatic geometric transformations in a cold strontium gas. *Nature communications* **9**, 3580 (2018).
10. A. A. Abdumalikov Jr *et al.*, Experimental realization of non-Abelian non-adiabatic geometric gates. *Nature* **496**, 482-485 (2013).
11. L. Faoro, J. Siewert, R. Fazio, Non-Abelian Holonomies, Charge Pumping, and Quantum Computation with Josephson Junctions. *Physical review letters* **90**, 028301 (2003).
12. T. Yan *et al.*, Experimental realization of nonadiabatic shortcut to non-Abelian geometric gates. *Physical review letters* **122**, 080501 (2019).
13. D. Leibfried *et al.*, Experimental demonstration of a robust, high-fidelity geometric two ion-qubit phase gate. *Nature* **422**, 412-415 (2003).
14. Y. Sekiguchi, N. Niikura, R. Kuroiwa, H. Kano, H. Kosaka, Optical holonomic single quantum gates with a geometric spin under a zero field. *Nature photonics* **11**, 309-314 (2017).
15. K. Nagata, K. Kuramitani, Y. Sekiguchi, H. Kosaka, Universal holonomic quantum gates over geometric spin qubits with polarised microwaves. *Nature communications* **9**, 3227 (2018).
16. S. Arroyo-Camejo, A. Lazariiev, S. W. Hell, G. Balasubramanian, Room temperature high-fidelity holonomic single-qubit gate on a solid-state spin. *Nature communications* **5**, 4870 (2014).
17. Z.-G. Chen, R.-Y. Zhang, C. T. Chan, G. Ma, Classical non-Abelian braiding of acoustic modes. *Nature Physics* **18**, 179-184 (2022).
18. O. You *et al.*, Observation of non-Abelian Thouless pump. *Physical Review Letters* **128**, 244302 (2022).
19. X.-L. Zhang *et al.*, Non-Abelian braiding on photonic chips. *Nature Photonics* **16**, 390-395 (2022).
20. Y.-K. Sun *et al.*, Non-Abelian Thouless pumping in photonic waveguides. *Nature Physics* **18**, 1080-1085 (2022).
21. V. Neef *et al.*, Three-dimensional non-Abelian quantum holonomy. *Nature Physics* **19**, 30-34 (2023).
22. M. Kremer, L. Teuber, A. Szameit, S. Scheel, Optimal design strategy for non-Abelian geometric phases using Abelian gauge fields based on quantum metric. *Physical Review Research* **1**, 033117 (2019).

23. V. Brosco, L. Pilozzi, R. Fazio, C. Conti, Non-Abelian Thouless pumping in a photonic lattice. *Physical Review A* **103**, 063518 (2021).
24. W. Song *et al.*, Shortcuts to adiabatic non-Abelian braiding on silicon photonic chips. *Science Advances* **11**, eadt7224 (2025).
25. Y. Chen *et al.*, High-dimensional non-Abelian holonomy in integrated photonics. *Nature Communications* **16**, 3650 (2025).
26. J. Noh *et al.*, Braiding photonic topological zero modes. *Nature Physics* **16**, 989-993 (2020).
27. Q. Lin, S. Fan, Light guiding by effective gauge field for photons. *Physical Review X* **4**, 031031 (2014).
28. Y. Lumer *et al.*, Light guiding by artificial gauge fields. *Nature Photonics* **13**, 339-345 (2019).
29. M. C. Rechtsman *et al.*, Photonic Floquet topological insulators. *Nature* **496**, 196-200 (2013).
30. E. Lustig *et al.*, Photonic topological insulator in synthetic dimensions. *Nature* **567**, 356-360 (2019).
31. L. He *et al.*, Floquet Chern insulators of light. *Nature Communications* **10**, 4194 (2019).
32. Z. Yang, E. Lustig, Y. Lumer, M. Segev, Photonic Floquet topological insulators in a fractal lattice. *Light: Science & Applications* **9**, 128 (2020).
33. W. Song *et al.*, Gauge - Induced Floquet Topological States in Photonic Waveguides. *Laser & Photonics Reviews* **15**, 2000584 (2021).
34. W. Song *et al.*, Dispersionless Coupling among Optical Waveguides by Artificial Gauge Field. *Physical Review Letters* **129**, 053901 (2022).
35. Z. Wang *et al.*, Artificial-gauge-field-based inverse design for wideband-flat power splitter and microring resonator. **4**, 016001 (2025).
36. X. Yi, H. Zeng, S. Gao, C. Qiu, Design of an ultra-compact low-crosstalk sinusoidal silicon waveguide array for optical phased array. *Optics Express* **28**, 37505-37513 (2020).
37. X. Yi *et al.*, Demonstration of an ultra-compact 8-channel sinusoidal silicon waveguide array for optical phased array. *Opt. Lett.* **47**, 226-229 (2022).
38. W. Ford, *Numerical Linear Algebra with Applications: Using MATLAB and Octave*. (Academic press, 2014).
39. G. H. Robert, *Integrated Optics: Theory and Technology*. (Springer, 1985).
40. Y. A. Vlasov, S. J. McNab, Losses in single-mode silicon-on-insulator strip waveguides and bends. *Optics express* **12**, 1622-1631 (2004).
41. S. Longhi, Coherent destruction of tunneling in waveguide directional couplers. *Physical Review A—Atomic, Molecular, and Optical Physics* **71**, 065801 (2005).
42. S. Longhi, Self-imaging and modulational instability in an array of periodically curved waveguides. *Opt. Lett.* **30**, 2137-2139 (2005).
43. E. Paspalakis, Adiabatic three-waveguide directional coupler. *Optics communications* **258**, 30-34 (2006).
44. S. Longhi, Adiabatic passage of light in coupled optical waveguides. *Physical Review E* **73**, 026607 (2006).
45. S. Longhi, G. Della Valle, M. Ornigotti, P. Laporta, Coherent tunneling by adiabatic passage in an optical waveguide system. *Physical Review B* **76**, 201101 (2007).
46. Y. Lahini *et al.*, Effect of Nonlinearity on Adiabatic Evolution of Light. *Physical Review Letters* **101**, 193901 (2008).
47. H. S. Hristova, A. A. Rangelov, G. Montemezzani, N. V. Vitanov, Adiabatic three-waveguide coupler. *Physical Review A* **93**, 033802 (2016).

48. P. Boross, J. K. Asbóth, G. Széchenyi, L. Oroszlány, A. Pályi, Poor man's topological quantum gate based on the Su-Schrieffer-Heeger model. *Physical Review B* **100**, 045414 (2019).
49. H. J. Bernstein, Must quantum theory assume unrestricted superposition? *Journal of Mathematical Physics* **15**, 1677-1679 (1974).
50. S. Bertini, S. L. Cacciatori, B. L. Cerchiai, On the Euler angles for SU (N). *Journal of mathematical physics* **47**, (2006).
51. T. Tilma, E. Sudarshan, Generalized Euler angle parametrization for SU (N). *Journal of Physics A: Mathematical and General* **35**, 10467 (2002).
52. W. Greiner, B. Müller, *Quantum mechanics: symmetries*. (Springer Science & Business Media, 2012).
53. M. Artin, P. H. Algebra, Englewood Cliffs, NJ, 1991. MR 92g 1.
54. D. H. Sattinger, O. L. Weaver, *Lie groups and algebras with applications to physics, geometry, and mechanics*. (Springer Science & Business Media, 2013), vol. 61.
55. J. K. Asbóth, L. Oroszlány, A. Pályi, *A short course on topological insulators*. (Springer, 2016), vol. 919.
56. M. Moralis-Pegios, G. Giamougiannis, A. Tsakyridis, D. Lazovsky, N. Pleros, Perfect linear optics using silicon photonics. *Nature Communications* **15**, 5468 (2024).
57. R. Burgwal *et al.*, Using an imperfect photonic network to implement random unitaries. *Optics Express* **25**, 28236-28245 (2017).
58. E. Zahedinejad, J. Ghosh, B. C. Sanders, High-Fidelity Single-Shot Toffoli Gate via Quantum Control. *Physical Review Letters* **114**, 200502 (2015).
59. H. L. Gevorgyan, N. V. Vitanov, Ultrahigh-fidelity composite rotational quantum gates. *Physical Review A* **104**, 012609 (2021).
60. Y. Shen *et al.*, Deep learning with coherent nanophotonic circuits. *Nature Photonics* **11**, 441-446 (2017).
61. B. Bai *et al.*, Microcomb-based integrated photonic processing unit. *Nature Communications* **14**, 66 (2023).
62. Z. Wang, L. Chang, F. Wang, T. Li, T. Gu, Integrated photonic metasystem for image classifications at telecommunication wavelength. *Nature Communications* **13**, 2131 (2022).
63. T. Fu *et al.*, Photonic machine learning with on-chip diffractive optics. *Nature Communications* **14**, 70 (2023).
64. F. Ashtiani, A. J. Geers, F. Aflatouni, An on-chip photonic deep neural network for image classification. *Nature* **606**, 501-506 (2022).

Acknowledgments: We thank the Center for Advanced Electronic Materials and Devices (AEMD) of Shanghai Jiao Tong University (SJTU) and Tianjin H-chip Technology for the support in device fabrication.

Funding:

National Key R&D Program of China grant 2023YFB2804702

Natural Science Foundation of China (NSFC) grant 62175151 and 62341508

Shanghai Municipal Science and Technology Major Project

Author contributions:

Conceptualization: XHG, YLC

Methodology: XHG, YLC

Investigation: XHG, YLC

Visualization: XHG, YLC, JLX, AH

Funding acquisition: XHG

Project administration: XHG

Supervision: XHG, IHW, YKS

Writing – original draft: XHG, YLC, JLX, AH

Writing – review & editing: XHG, YLC, IHW, YKS

Competing interests: Authors declare that they have no competing interests

Data and materials availability: The data that support the plots within this paper are available from the corresponding authors upon request.

Supplementary Materials

Materials and Methods

Supplementary Text

Figs. S1 to S14

Tables S1

References (1–15)

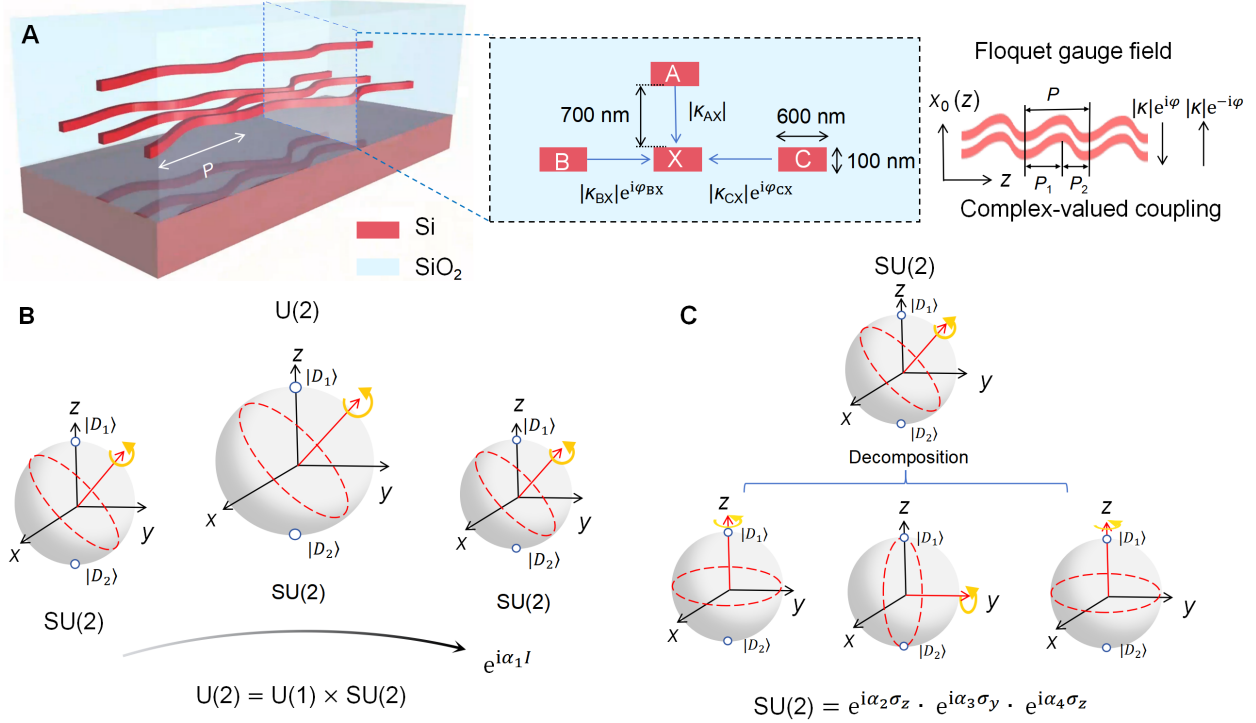


Fig. 1. Generic U(2) holonomy. (A) Structure of U(2) holonomy device. The device is comprised of four periodic bent silicon waveguides A, B, C, and X on two layers. All four waveguides have an identical bending profile $x_0(z)$. Thus, the coupling between waveguides B and X, C and X are complex-valued due to the induced AGF. The adiabatic evolution of complex-valued coupling can be precisely controlled by slowly varying the amplitude, period as well as profile of bending. (B)-(C) Illustration and decomposition of U(2) rotation in the Bloch sphere. (B) U(2) group can be decomposed as the product of $e^{i\alpha I}$ and SU(2) group. (C) SU(2) group can be further decomposed as the rotation around the z-axis, y-axis, and z-axis.

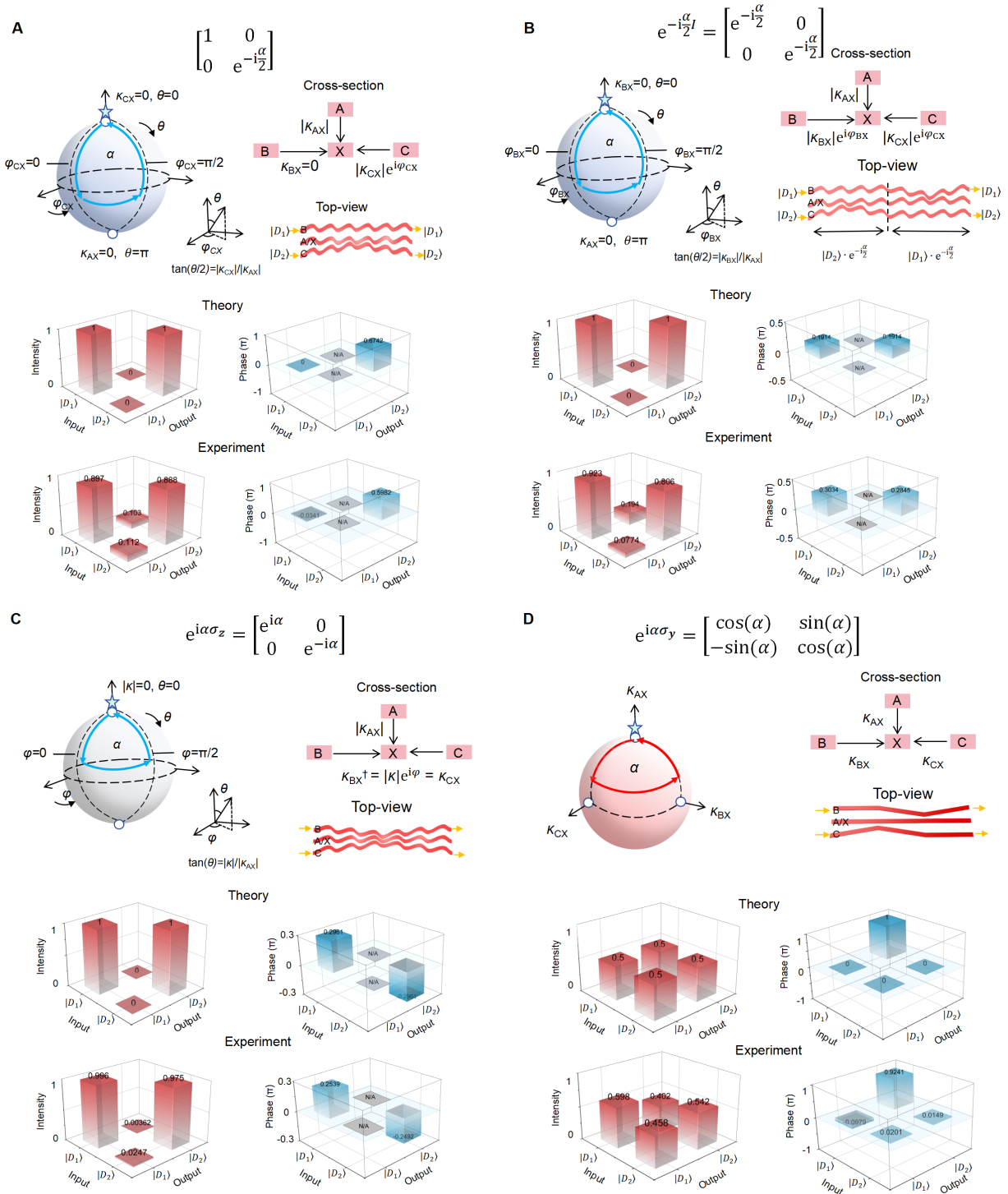


Fig. 2. Experimental results, theoretical prediction, holonomic paths in Hilbert space as well as structures in real space for different building blocks of $U(2)$ transformation. (A) $\begin{bmatrix} 1 & 0 \\ 0 & e^{-i\frac{\alpha}{2}} \end{bmatrix}$, $|D_1\rangle$ resides in an isolated waveguide, $|D_2\rangle$ acquires the Berry phase $-\frac{\alpha}{2}$ after experiencing two STIRAPs with complex-valued coupling. The detailed parameters can be found in Fig. S8A. (B)

$e^{-i\frac{\alpha}{2}I} = \begin{bmatrix} e^{-i\frac{\alpha}{2}} & 0 \\ 0 & e^{-i\frac{\alpha}{2}} \end{bmatrix}$, $|D_1\rangle$ also acquires the Berry phase $-\frac{\alpha}{2}$ after experiencing two STIRAPs with complex-valued coupling. The detailed parameters can be found in Fig. S8B. **(C)** $e^{i\alpha\sigma_z} = \begin{bmatrix} e^{i\alpha} & 0 \\ 0 & e^{-i\alpha} \end{bmatrix}$, the structure is designed as $g_{BX} = g_{CX}$ and $\kappa_{BX} = \kappa_{CX}^\dagger$. Two degenerate modes $|D_1\rangle$ and $|D_2\rangle$ acquire Berry phases with identical absolute values but opposite signs. The detailed parameters can be found in Fig. S8C. **(D)** $e^{i\alpha\sigma_y} = \begin{bmatrix} \cos(\alpha) & \sin(\alpha) \\ -\sin(\alpha) & \cos(\alpha) \end{bmatrix}$, which belongs to $SO(2)$ and has been demonstrated in many reported schemes. Three positive-valued couplings are isomorphic to a 2-sphere, α is the solid angle enclosed by the holonomic path.

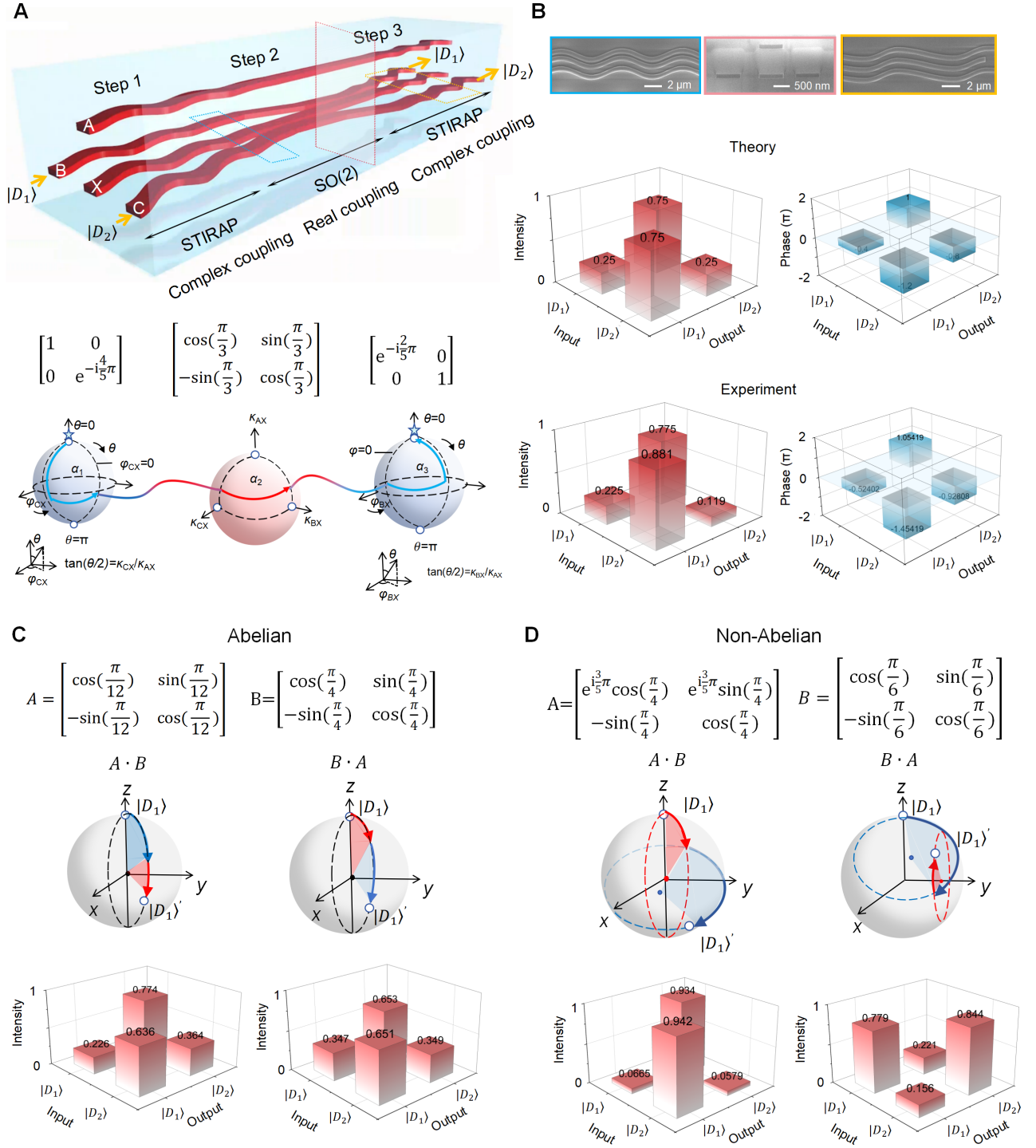


Fig. 3. Experimental results of a U(2) holonomy that involved different kinds of rotations, and the demonstration of non-Abelian characteristics. (A)-(B) A U(2) holonomy device that involved different kinds of rotations. **(A)** The structure in real space and the holonomic path in Hilbert space. **(B)** Experimental results and theoretical prediction. The insets are scanning electron microscope (SEM) figures and the focused ion beam (FIB) image in top-view and cross-sectional view, respectively. **(C)-(D)** Demonstration of the non-Abelian characteristic. **(C)** Cascading of two

SO(2) rotations ($e^{i\alpha\sigma_y}$), which are Abelian. **(D)** Cascading of a U(2) rotation and a SO(2) rotation, they are non-Abelian.

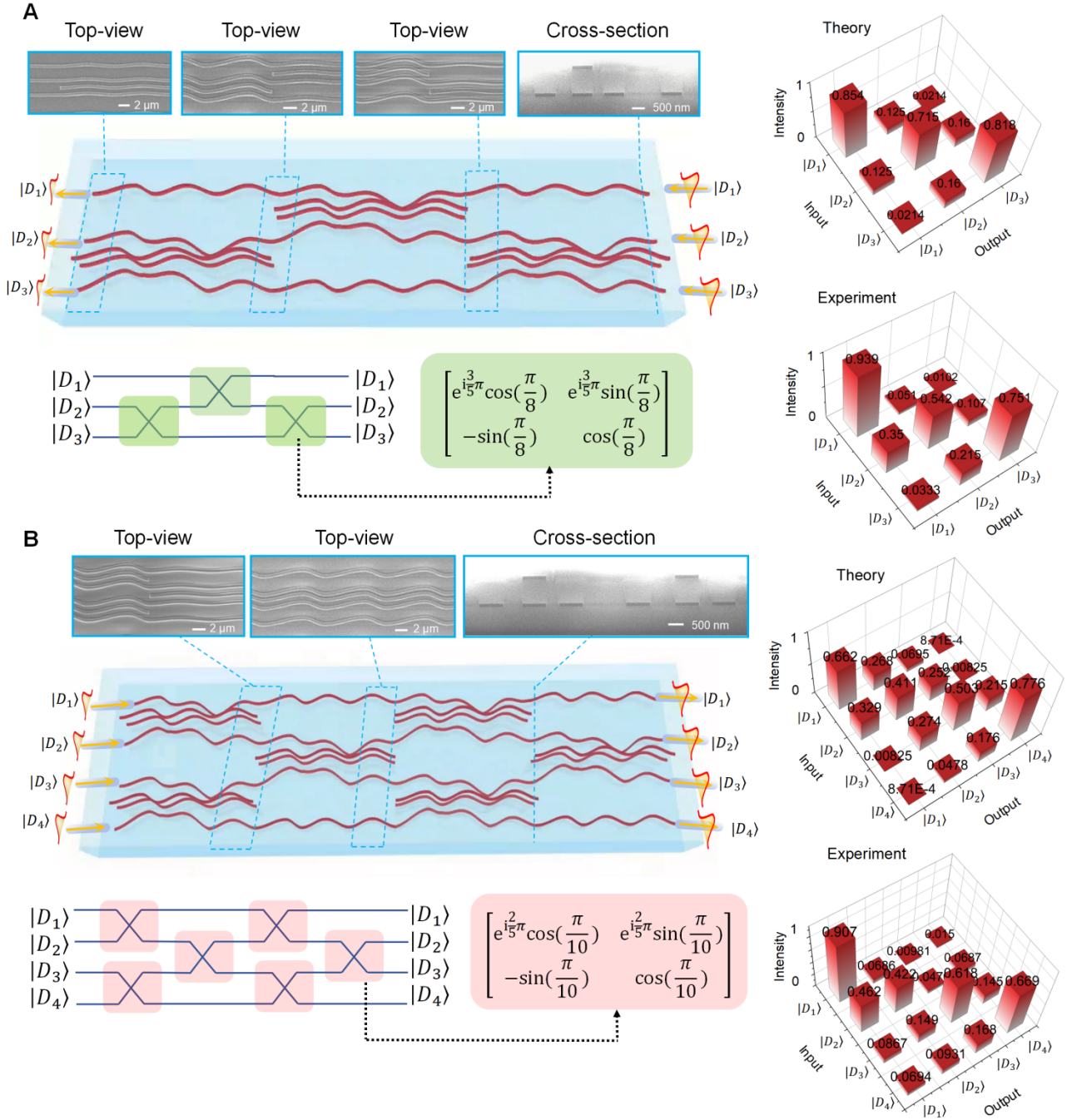


Fig. 4. Experimental results of U(3) and U(4) holonomy. (A) U(3) holonomy. The experimentally measured and theoretically predicted intensity, structure, as well as the mathematical model are shown. The insets are SEM figures and the FIB image in top-view and cross-sectional view, respectively. (B) U(4) holonomy. The experimentally measured and theoretically predicted intensity, structure, as well as the mathematical model are shown. The insets are SEM figures and the FIB image in the top-view and cross-sectional view, respectively.